Supplemental Materials: Magnetophoretic modulation of $BaSO_4$ scaling: laboratory investigation and industrial case study

M. ElMassalami,[1,*] G. G. Silva,[1] M. R. da Silva,[1] A. Elzubair,[2] J. C. Queiroz Neto,[3] and N. M. Pinhal[1]

[1] *Instituto de Fisica, Universidade Federal do Rio de Janeiro, Caixa Postal 68528, 21945-972 Rio de Janeiro, Brazil*

[2] *Military Institute of Engineering, Praça General Tibúrcio 80, 22290-270, Urca, Rio de Janeiro, RJ, Brazil*

[3] *Departamento de Engenharia Química e de Petróleo, Universidade Federal Fluminense, Rio de Janeiro, RJ, Brazil*

(Dated: July 10, 2026)

In these supplemental materials, we provide the theoretical, experimental, and complementary analytical basis for the proposed magnetophoretic modulation of $BaSO_4$ scaling. We first distinguish the Lorentz/Faraday–Hall response of the ionic electrolyte from the magnetic-gradient force acting on magnetizable contaminants, showing that the former is not expected to measurably affect homogeneous nucleation and growth, whereas the latter can promote NMP agglomeration and heterogeneous template formation. We then describe the laboratory and industrial setups, the paired field/zero-field comparison criterion, and the limitations of conductivity and turbidity as *in situ* probes. Complementary XRD, SEM/EDS, magnetization, and susceptibility analyses are presented to support the interpretation that magnetic-field gradients act mainly through heterogeneous, particulate-assisted pathways. Finally, an industrial-scale case study illustrates how field-gradient effects can modify phase composition, magnetic response, and scale evolution along a production line.

SM1. Two magnetic-force mechanisms and their influence on nucleation and growth processes[1]

In typical laboratory, domestic, or industrial anti-scale magnetic treatment (ASMT) setups, a time-independent magnetic field is applied to a flowing, supersaturated, scale-prone fluid. Such *supersaturated contaminant-bearing fluid* can be conceptually separated into two components, as illustrated in Fig. SM1: (i) an electrolyte, i.e., an ion-bearing solution, as shown in Fig. SM1(a), and (ii) a suspension of contaminants, as shown in Fig. SM1(b).

Within the magnetic zone, the applied field may be decomposed as $\mathbf{H} = \mathbf{H}_{dc} + \mathbf{H}_r$, where $\mathbf{H}_{dc}$ denotes the uniform component and $\mathbf{H}_r$ the spatially varying component, for which $\nabla H \neq 0$. In such a two-component fluid, two magnetic-force mechanisms are relevant: the Lorentz force, which acts on the ionic subsystem through $\mathbf{H}$, and the magnetic-gradient force, which acts on magnetizable particulates through the spatially nonuniform field component.

A. Lorentz force on the ionic subsystem [Fig. SM1(a)]

For ionic species of charge number z_i and molar concentration C_i moving with average velocity $\mathbf{v}$ through a magnetic field $\mathbf{H}$, the Lorentz-force density can be written as[3–6]

$$\mathbf{f}_{L,i} = z_i C_i F\, \mathbf{v} \times \mathbf{H}, \tag{SM1}$$

where F is Faraday's constant. This force drives positive and negative ions toward opposite sides of the tube, producing only a negligible charge accumulation at the boundary. The resulting charge separation generates an internal electric force, $q\mathbf{E}$, which rapidly counterbalances the Lorentz force [Fig.SM1(a)].[3,4,7–14] At equilibrium, the net force on the ions vanishes, yielding a steady boundary charge distribution and an induced electromotive response that is largely composition-independent, without any significant change in the bulk ionic concentration.

This balance between the Lorentz force and the induced electric force suggests that, under our conditions, the direct Lorentz-force contribution is unlikely to measurably affect the ion-activity product, a_{ap}.[7] Accordingly, it is also unlikely to alter the thermodynamic driving force for *homogeneous* nucleation or, by extension, homogeneous growth kinetics. For a homogeneous precipitation process, such as that of $BaSO_4$ or $CaCO_3$, the thermodynamic driving force is governed by the supersaturation state,

$$\frac{\Delta\mu}{k_B T} = \ln\left(\frac{a_{ap}}{K_{sp}^{eq}}\right), \tag{SM2}$$

* massalam@if.ufrj.br

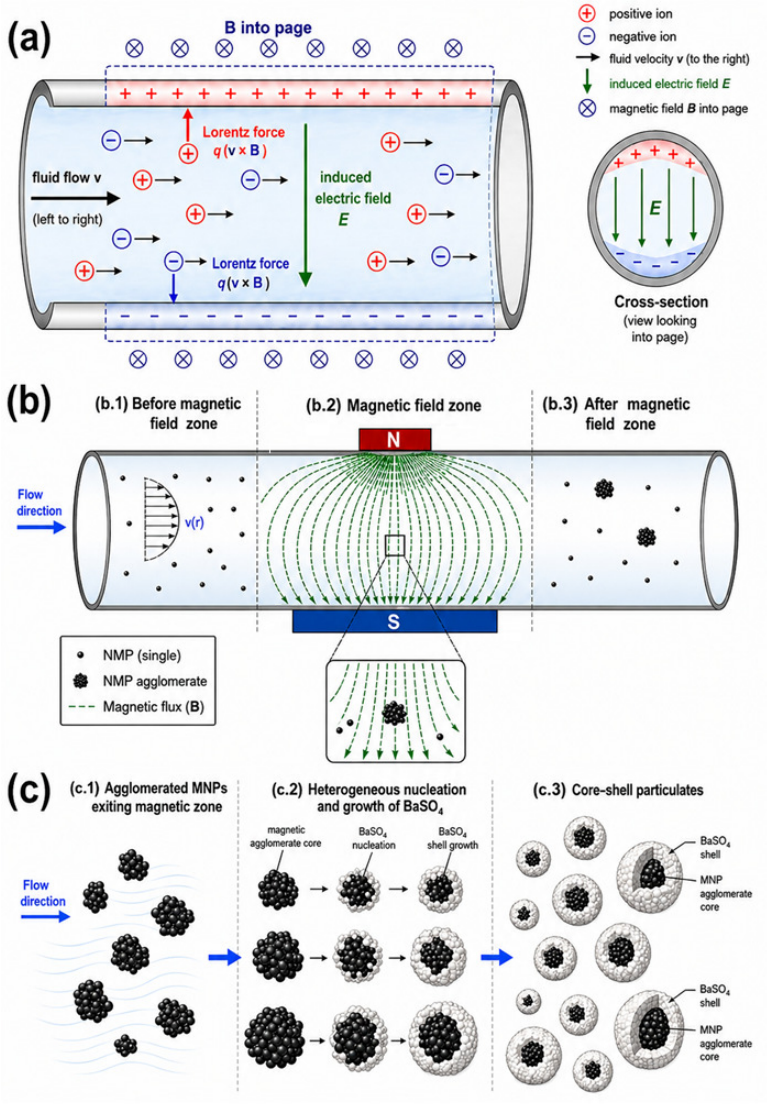

FIG. SM1. Schematic illustration of the magnetically induced processes considered in this work. **(a)** Magnetically induced ionic charge separation in a flowing electrolyte through a cylindrical tube while a magnetic field, $\mathbf{B}$,[2] is applied perpendicular to the flow direction. The circular inset shows the cross-sectional view of the tube looking into the flow direction.
(b) Influence of a magnetic-field gradient on ferromagnetic-like nanomagnetic particles (NMPs) dispersed in the flowing fluid, with the velocity distribution indicated in the inset. Three regions are envisaged: (b.1) before the magnetic-field zone, where the NMPs are mostly dispersed; (b.2) within the magnetic-field zone, where only the magnetic flux is shown—intentionally exaggerated to illustrate a strong magnetic-field gradient—and no NMPs are displayed (see the expanded view); and (b.3) after the magnetic-field zone, where both residual single NMPs and NMP-agglomerates are present. The expanded view shows the local magnetic flux threading an infinitesimal fluid element embedded in a cylindrically symmetric flow. Since the local velocity within this element can be treated as approximately uniform and constant, and since acceleration, shear, and rotational effects are assumed to be negligible over the relevant length and time scales, the processes occurring inside the element may be described in an approximately inertial reference frame moving with it. Within this element, the field gradient polarizes and orients the NMPs, thereby promoting their mutual magnetic attraction. As discussed in the main text, this local magnetic interaction can lead to NMPs agglomeration and partial stabilization, provided that it competes effectively with the opposing effects of hydrodynamic drag and Brownian motion.
(c) Proposed post-magnetic-zone pathway for the agglomerated MNPs and their role in heterogeneous nucleation and growth. In (c.1), the MNP-agglomerates that survive the hydrodynamic forces are swept downstream after exiting the magnetic-field zone, together with remaining unagglomerated MNPs (not shown). In (c.2), these magnetic agglomerates act as templates for heterogeneous nucleation and subsequent growth of supersaturated $BaSO_4$. In (c.3), the resulting particulates are envisaged as core–shell structures, with an MNP-agglomerate core surrounded by a diamagnetic $BaSO_4$ shell. A distribution of both core size and shell thickness is expected in the final population of core–shell particulates.

where K_{sp}^{eq} is the equilibrium solubility product.[15,16] Thus, if a uniform magnetic field does not measurably change a_{ap}, conductivity, or pH, as observed under the present conditions and in Refs. 1, it does not measurably alter $\Delta\mu$ and, consequently, the thermodynamic driving force for homogeneous nucleation.

The same reasoning applies to the main kinetic quantities of the homogeneous process, since the nucleation rate, R_N, induction time, τ_{ind}, and rough-face growth rate, R_G, are primarily controlled by the same supersaturation measure:[15]

$$R_N \approx K_1 \exp\left[-\frac{K_2}{\ln\left(a_{ap}/K_{sp}^{eq}\right)}\right], \qquad \tau_{ind} \approx \frac{K_3}{\left[\ln\left(a_{ap}/K_{sp}^{eq}\right)\right]^2 a_{ap}}, \qquad R_G \approx K_4\left(a_{ap} - K_{sp}^{eq}\right), \tag{SM3}$$

where K_1–K_4 are taken to be field-independent prefactors under the present conditions.

Within Classical Nucleation Theory,[15] the same supersaturation dependence determines the critical diameter, d_c, corresponding to the maximum of the homogeneous nucleation barrier. Clusters larger than d_c tend to grow spontaneously. For a spherical $BaSO_4$ nucleus,

$$d_c = \frac{4\sigma V_m}{k_B T \ln S} \propto \frac{1}{\ln S}, \qquad \text{with} \qquad S = \sqrt{\frac{a_{ap}}{K_{sp}}}, \tag{SM4}$$

where σ is the $BaSO_4$/solution interfacial energy, V_m is the molecular volume of $BaSO_4$ in the crystal, k_B is the Boltzmann constant, T is the absolute temperature, and S is the supersaturation ratio. For fixed experimental conditions, the factor $4\sigma V_m/(k_B T)$ is constant. Since $d_c \propto 1/\ln S$, the critical size decreases rapidly with increasing supersaturation. Under highly supersaturated and non-equilibrium conditions, such as rapid mixing of concentrated barium and sulfate streams, the nucleation barrier is strongly reduced and d_c may fall within the sub-nanometer to few-nanometer range, corresponding to clusters containing only a few tens to hundreds of ionic units. Within the present argument, these homogeneous-nucleation estimates remain magnetic-field independent.

B. Magnetic-gradient force on magnetizable particulates [Fig. SM1(b)]

For suspended entities with molar susceptibility χ_m and molar concentration C in a nonuniform magnetic field, the magnetic-gradient force density can be written, to leading order, as[5,17,18]

$$\mathbf{f}_{\nabla H} \simeq \nabla\left(\frac{\mu C \chi_m}{2} H^2\right), \tag{SM5}$$

where μ is the permeability of the medium. For particles with positive magnetic-susceptibility contrast relative to the surrounding liquid, such as ferromagnetic or ferrimagnetic particulates, this force drives magnetophoretic motion toward regions of higher field intensity.[19] To rationalize the local action of this force in the flowing fluid, we consider, in Fig.SM1(b), a cylindrically symmetric velocity distribution and focus on an infinitesimal fluid element moving with a locally uniform velocity through an otherwise weakly diamagnetic background. Within this element, the field gradient polarizes and orients the NMPs, inducing magnetophoretic drift and promoting their mutual magnetic attraction, which can lead to agglomeration. Thus, the relevant process is not necessarily the macroscopic migration of either the fluid element or the NMPs across the entire magnetic zone toward the strongest-field region. Rather, it is the local polarization, alignment, and aggregation of magnetically responsive particulates within a small fluid element threaded by the magnetic flux.

Thus, the magnetophoretic response can drive local particle assembly and coalescence into larger magnetic agglomerates, which may then act as heterogeneous nucleation templates for subsequent scalant deposition, as schematically shown in Fig. SM1(c). In this picture, the resulting particulates are expected to develop a core–shell morphology, with a magnetic agglomerate core surrounded by a diamagnetic scale shell. Because both the initial contaminant population and the agglomeration process are size-distributed, a corresponding distribution of core sizes and shell thicknesses is also expected.

This mechanism is fundamentally different from the Lorentz-force response of the ionic subsystem discussed in § SM1 A. The Lorentz force is rapidly balanced by the induced Faraday–Hall electric field and does not measurably modify the bulk ion-activity product. By contrast, the magnetic-gradient force acts directly on magnetically responsive particulates and can promote their redistribution, alignment, and agglomeration.

C. Paired field/zero-field comparison

The above analysis provides a natural distinction between the zero-field and field-applied cases. It motivated us to apply, consistently throughout this study, a paired field/zero-field comparison in which otherwise identical

experiments were performed with and without an applied magnetic field. This comparison isolates the magnetic contribution, since all nonmagnetic factors affecting nucleation and growth are common to both cases and can therefore be filtered out during the comparison. As an illustration, in the absence of an applied magnetic-field gradient, precipitation may proceed through a combination of homogeneous and nonmagnetic heterogeneous nucleation and growth. In the presence of an applied field gradient, however, an additional heterogeneous pathway becomes available (see Fig.SM1(b-c)): magnetically responsive particulates are polarized, aligned, and agglomerated by the field gradient, forming templates that can lower the effective barrier for heterogeneous nucleation and promote subsequent growth. Thus, any significant magnetic influence on precipitation is expected to arise mainly from magnetic-gradient forces, magnetophoretic aggregation, or magnetically responsive contaminants, rather than from a direct modification of bulk homogeneous nucleation.

Our empirical results, discussed in the main text, are consistent with this distinction/interpretation. Under otherwise identical experimental conditions, the structural, magnetic, elemental, and morphological analyses differ markedly between the cases with and without an applied magnetic-field gradient. We therefore interpret the field-applied case as involving a magnetically activated heterogeneous pathway, in which magnetophoretically agglomerated NMPs act as templates for $BaSO_4$ nucleation and growth. We further assume that the lower-bound size of these magnetically agglomerated templates is comparable to, or larger than, the homogeneous critical diameter d_c estimated in Eq. SM4.

D. Field-driven NMP agglomeration and template stability under competing hydrodynamic and Brownian forces

The above description raises two related questions: how can NMPs agglomerate in a recirculating system subject to Brownian motion, viscous drag, mechanical agitation, and centrifugal pumping; and, if such agglomerates form, how can they remain sufficiently stable to act as templates for heterogeneous nucleation and growth?

At present, our answer is primarily phenomenological. In the paired field/zero-field comparison, Brownian diffusion, viscous drag, mechanical agitation, and pumping are present in both experiments. Therefore, the marked differences observed in the magnetization curves, as well as in the *ex situ* structural and morphological analyses, are most naturally associated with the applied magnetic-field gradient. Within the framework of Figs. SM1(b,c), these observations imply that magnetic polarization and local NMP aggregation can withstand the competing dispersive effects over the relevant experimental time scales; otherwise, no field-dependent *ex situ* differences would be observed. In a magnetophoretic Péclet-number picture, this means that the effective magnetic contribution to particle assembly is sufficiently large to compete with, and likely exceed, diffusive randomization under the conditions where field-dependent morphology and magnetization are observed. Thus, the relevant magnetophoretic Péclet number is expected to be larger than unity.

Within this framework, the proposed mechanism may be summarized as follows. Inside an infinitesimal fluid element, the magnetic-field gradient polarizes the NMPs. The polarized particles then interact magnetically, align along the local magnetic flux, and attract one another, forming small oriented agglomerates. Among these, the agglomerates that successfully act as templates for the onset of nucleation and growth become further stabilized by the deposited scalant phase. This produces a positive feedback process, analogous to crystal growth on a stable nucleus: once deposition begins, the growing shell increases the effective size and persistence of the aggregate, helping it withstand Brownian and hydrodynamic effects that would otherwise disorient or redisperse it. This feedback-stabilized agglomeration provides the physical basis for the magnetic-template mechanism proposed in Fig. SM1.

This discussion strengthens the mechanistic basis of our interpretation while preserving its phenomenological character. A quantitative evaluation of the competing magnetic, Brownian, viscous, and hydrodynamic forces under the actual experimental conditions would be highly desirable and represents an important next step in the investigation of this magnetohydrodynamic precipitation process.

SM2. Structural robustness, morphologies, and nucleation–growth pathways in $BaSO_4$

The crystal structure of $BaSO_4$ (barite) is orthorhombic (space group *Pnma*). Ba^{2+} cations form a dense framework bonded to strongly covalent $SO_4{}^{2-}$ tetrahedra, yielding a rigid, close-packed, chemically stable structure. These attributes underlie both the tenacity of $BaSO_4$ scaling and its widespread use in drilling fluids.

The barite P–T phase diagram is well established within $P < 10\,\mathrm{GPa}$ and $T < 1000^{\circ}\mathrm{C}$.[20–22] The barite phase is retained in $BaSO_4$ scale across broad growth conditions—ionic strength, supersaturation, temperature, pH, additives, and field—with negligible impact on lattice symmetry or metrics.

$BaSO_4$ scaling—often triggered by mixing incompatible waters—can proceed via homogeneous nucleation in the bulk or heterogeneous nucleation on preexisting surfaces. The dominant pathway is governed by supersaturation, availability of foreign surfaces, magnetic field, pH, temperature, and pressure, which together control both the rate of

TABLE SM1. Representative experiments and conditions: For each run, Si_{eq}, we list: index (i=7-8,10-17); reaction route (eq =Eqs.1,2); magnetic field (H = 0 or 8 kOe); Fe-based contaminant (mol % of Fe_2O_3 or Fe_2O_3 NP relative to Ba); filter pore size ($7, 8\,\mu$m); and the corresponding figure (Fig#). *In situ*: $\sigma_{i,eq}$ and $pH_{i,eq}$ denote conductivity and pH; turbidity was not measured for runs i=1-18. Magnetization: Mi_H and Mi_L are isotherms at 300 K and 15 K; χi_C and χi_W are susceptibilities on cooling and warming. XRD: Rietveld-refined unit-cell parameters (a, b, c). SEM/EDS: micrographs and stoichiometric coefficients (mole fractions of S, O, and Fe normalized to Ba). The final two columns give the total normalized mass percentage of all impurities ("Other") and of Fe ("Fe"). Because EDS is less sensitive to light elements, O and S values are qualitative.

Sample #	H [kOe]	Fe_2O_3 %	Fe_2O_3 NP %	Filt [μm]	σ [mS/cm]	pH	M_H [memu/g]	M_L [memu/g]	χ_C [μemu/g]	χ_W [μemu/g]	XRD	a [Å]	b [Å]	c [Å]	SEM	Ba stoichiom.	S coeff.	O	Fe	Other norm.	Fe mass
Fig.#	nominal				SM2(a)	SM2(b)	SM5(a)	SM5(b)	SM5(c)	SM5(d)	SM3	± 0.0001 Å			SM6					%.	
$S7_{eq1}$	0	1	0	8	$\sigma 7_{eq1}$	$pH7_{eq1}$	$M7_H$	$M7_L$	$\chi 7_C$	$\chi 7_W$	(g)	8.877	5.4543	7.1532	-	1	0.7	2.5	0.001	1.5	0.03
$S8_{eq1}$	8	1	0	8	$\sigma 8_{eq1}$	$pH8_{eq1}$	$M8_H$	$M8_L$	$\chi 8_C$	$\chi 8_W$	(h)	8.87684	5.454	7.1534	-	1	0.8	3.1	0.002	0.8	0.05
$S10_{eq1}$	8	1	0	8	$\sigma 10_{eq1}$	$pH10_{eq1}$	$M10_H$	$M10_L$	$\chi 10_C$	$\chi 10_W$	(j)	8.8788	5.4547	7.1544	(c)	1	0.8	3.9	0.000	0.4	0.0
$S11_{eq1}$	8	1	0	8	$\sigma 11_{eq1}$	$pH11_{eq1}$	$M11_H$	$M11_L$	$\chi 11_C$	$\chi 11_W$	(k)	8.8769	5.4545	7.1532	(d)	1	0.9	3.4	0.006	0.6	0.2
$S12_{eq2}$	0	0	0	7	$\sigma 12_{eq2}$	$pH12_{eq2}$	$M12_H$	$M12_L$	$\chi 12_C$	$\chi 12_W$	(l)	8.8789	5.4566	7.1554	-	1	0.8	2.7	0.001	0.54	0.03
$S13_{eq2}$	0	0	0	7	$\sigma 13_{eq2}$	$pH13_{eq2}$	$M13_H$	$M13_L$	$\chi 13_C$	$\chi 13_W$	(m)	8.878	5.4550	7.1543	-	1	0.8	3.8	0.001	.45	0.01
$S14_{eq2}$	0	0	0	7	$\sigma 14_{eq2}$	$pH14_{eq2}$	$M14_H$	$M14_L$	$\chi 14_C$	$\chi 14_W$	(n)	8.8779	5.4550	7.1540	(a)	1	0.9	2.9	0.002	0.22	0.06
$S15_{eq2}$	8	0	0	7	$\sigma 15_{eq2}$	$pH15_{eq2}$	$M15_H$	$M15_L$	$\chi 15_C$	$\chi 15_W$	(o)	8.8780	5.4552	7.1541	(b)	1	0.8	3.3	0.003	0.5	0.1
$S16_{eq2}$	0	0	5.5	7	$\sigma 16_{eq2}$	$pH16_{eq2}$	$M16_H$	$M16_L$	$\chi 16_C$	$\chi 16_W$	(p)	8.8780	5.4555	7.1547	(e)	1	0.9	2.5	0.005	0.4	0.1
$S17_{eq2}$	8	0	5.5	7	$\sigma 17_{eq2}$	$pH17_{eq2}$	$M17_H$	$M17_L$	$\chi 17_C$	$\chi 17_W$	(q)	8.8772	5.4552	7.1536	(f)	1	0.7	1.6	0.15	7	4

scale formation and the resulting morphology and adhesion. Homogeneous nucleation, favored at high supersaturation, yields numerous, finer, more uniformly sized particles with fibrous or dendritic character; heterogeneous nucleation, competitive at lower supersaturation, yields fewer, larger particles with broader size distributions. Additives can selectively stabilize or destabilize specific crystallographic faces, while pH and temperature tune overall and face-selective growth kinetics. Resulting morphologies reflect relative surface energies: higher-energy faces grow faster and vanish, leaving lower-energy faces or those whose energy is reduced by selective additive adsorption.[23–28]

Additives play a pivotal role in $BaSO_4$ scaling and typically fall into three categories: (i) deliberately dosed (e.g., chemical inhibitors[29–33]) or inadvertently introduced (e.g., via injected fluids in secondary recovery); (ii) corrosion-derived products from engineered components such as pipelines and pumps;[30,34] and (iii) species leached during prolonged contact with transition–metal–bearing minerals.[34] Common contaminants/additives include iron and alkaline-earth cations as well as potentially magnetic transition-metal or rare-earth ions. Ferrous iron is among the most prevalent contaminant cations in produced waters,[29] and Fe^{2+}/Fe^{3+} concentrations can span 10^{-5}–10^{-3} M depending on geological and engineering specifics.[30] Although iron can form its own scales, scarcity usually limits direct fouling; more consequential is its interfacial role: when compatible with barite surface chemistry, iron can adsorb selectively on low–surface–energy faces, modulating inhibitor performance and growth kinetics.[29–33]

SM3. Experimental setups and procedures

A. Laboratory-scale setup

Figure SM2(a) shows a closed-loop flow circuit that drives Na_2SO_4(aq) from a temperature-controlled reservoir through a nonconductive polycarbonate flow cell positioned between electromagnet poles. The setup follows Ref. 1, with the addition of a turbidity sensor (see below). To avoid bubble- and turbulence-induced artifacts that would arise if the turbidimeter were placed in the reservoir, turbidity is measured in a dedicated side cell continuously supplied by a peristaltic pump. Methods and procedures are as described in the main text (see also Ref. 1). Briefly, after 10 min of baseline circulation, a Ba^{2+} source—$BaCl_2$(aq) or $BaCl_2 \cdot 2H_2O$—is metered by a peristaltic pump for 40 min to achieve $BaSO_4$ supersaturation; the main circulation then continues for 50 min. Inline and in-tank probes record conductivity, pH, temperature, pressure, flow, turbidity, and electrode potentials.

The turbidity sensor uses a 90° light-scattering geometry with an infrared LED source and is sensitive to the presence of suspended particles through the intensity of the scattered light. However, it provides an integrated turbidity signal rather than a direct particle-size distribution. Its response depends not only on particle concentration, but also on particle size, shape, refractive index, and aggregation state. Therefore, it is useful for detecting changes in the overall suspended-particle loading, especially *in situ* or under flow conditions, but it cannot reliably resolve individual particle sizes or distinguish a large number of small particles from a smaller number of larger aggregates.

This limitation can be addressed more directly using an Optical Particle Size Analyzer, which is also a real-time optical probe of suspended matter, but measures different properties of the suspension. For example, a dynamic image-analysis system operating in liquid media can directly image individual particles or aggregates and provide quantitative particle-size and shape distributions above its optical-resolution limit. Torraca[36] used this technique to monitor, *in situ*, the evolution of both the concentration and average diameter of precipitated $CaCO_3$ particles, with

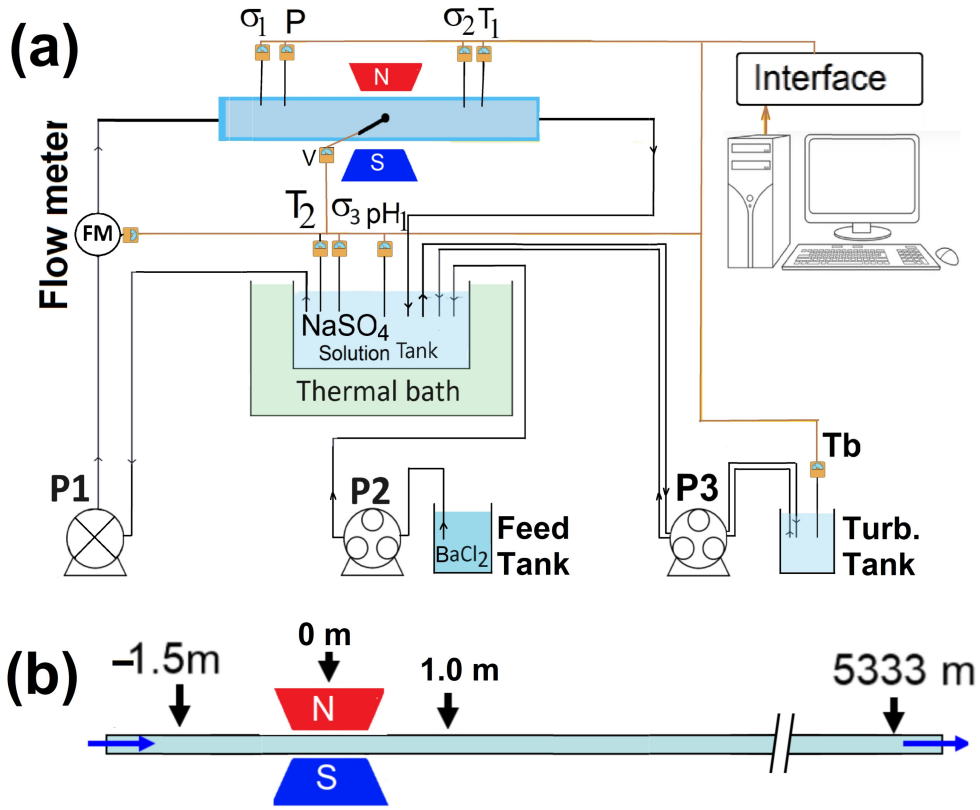

FIG. SM2. Schematics of the experimental setups used in this work. **(a)** Purpose-built, computer-interfaced laboratory apparatus comprising hydraulic, control, sensors, and data-acquisition subsystems. A nonconductive polycarbonate flow cell (cylindrical, 5 cm diameter, 30 cm length; shown in light-blue) is positioned between the poles of an electromagnet ($|\vec{H}| \leq 10$ kOe) and connected via 3/4-in braided tubing to a 12.7 L reservoir containing a solution of Na_2SO_4 dissolved in distilled water ($\sigma \approx 2\,\mu$S cm^{-1}). Temperature is regulated by thermal contact with a thermal bath and a closed-loop water-cooling stainless-steel coil inside the reservoir. Initially, the Na_2SO_4(aq) solution (7.306 mM) is circulated by a centrifugal pump P_1 (56 L min^{-1}). After 10 min, a Ba^{2+} source—$BaCl_2$(aq) or $BaCl_2 \cdot {}_2H_2O$(aq)—is dosed by a peristaltic pump P_2 (25 mL min^{-1} for 40 min). Afterwards, P_1 circulation continues for 50 min. Probes placed in the cell, line, and reservoir monitor conductivity (σ_i), pH (pH_i), temperature (T_i), pressure (P), flow (FM), turbidity (Tb), and a pair of electrodes. To minimize settling and ensure homogeneous sampling in the turbidity loop, agitation is maintained at 500 (reservoir), 300 (feed), and 100 (turbidity cell) rpm. **(b)** Schematic of the >6 km production line. Unfortunately, the installed tubing and infrastructure do not allow the installation of in-situ monitoring techniques, such as conductivity, pH, or turbidity sensors. The influence of the magnetic field could only be evaluated through ex-situ analyses of scale samples collected from the three available access points. These sample batches were collected at positions measured relative to the magnetic-field-generating device, located at 0 m: −1.5 m upstream, +1.0 m downstream, and +5331 m farther downstream. These three sampling points were used to track the evolution of the precipitation process along the production line.

and without an applied magnetic field. The corresponding evolution of particle concentration and average size is shown in the adapted Fig.SM8. In the zero-field case, Fig.SM8(a) shows that, after an induction period, the optical particle concentration increases as micrometric $CaCO_3$ particles begin to form. As aggregation and precipitation proceed, the number of suspended particles eventually decreases, producing a maximum in C_{opt} followed by a gradual decline. In contrast, the zero-field average diameter, shown in Fig.SM8(b), increases monotonically and continues to grow even after the end of the $CaCl_2$ addition period. With an applied magnetic field, Fig.SM8(a) indicates an earlier onset of particle formation, consistent with magnetophoretically driven agglomeration of magnetic contaminants. These induced agglomerates can additionally act as heterogeneous nucleation centers, thereby shortening the induction time relative to the zero-field case (see § SM1 B and Fig.SM1).

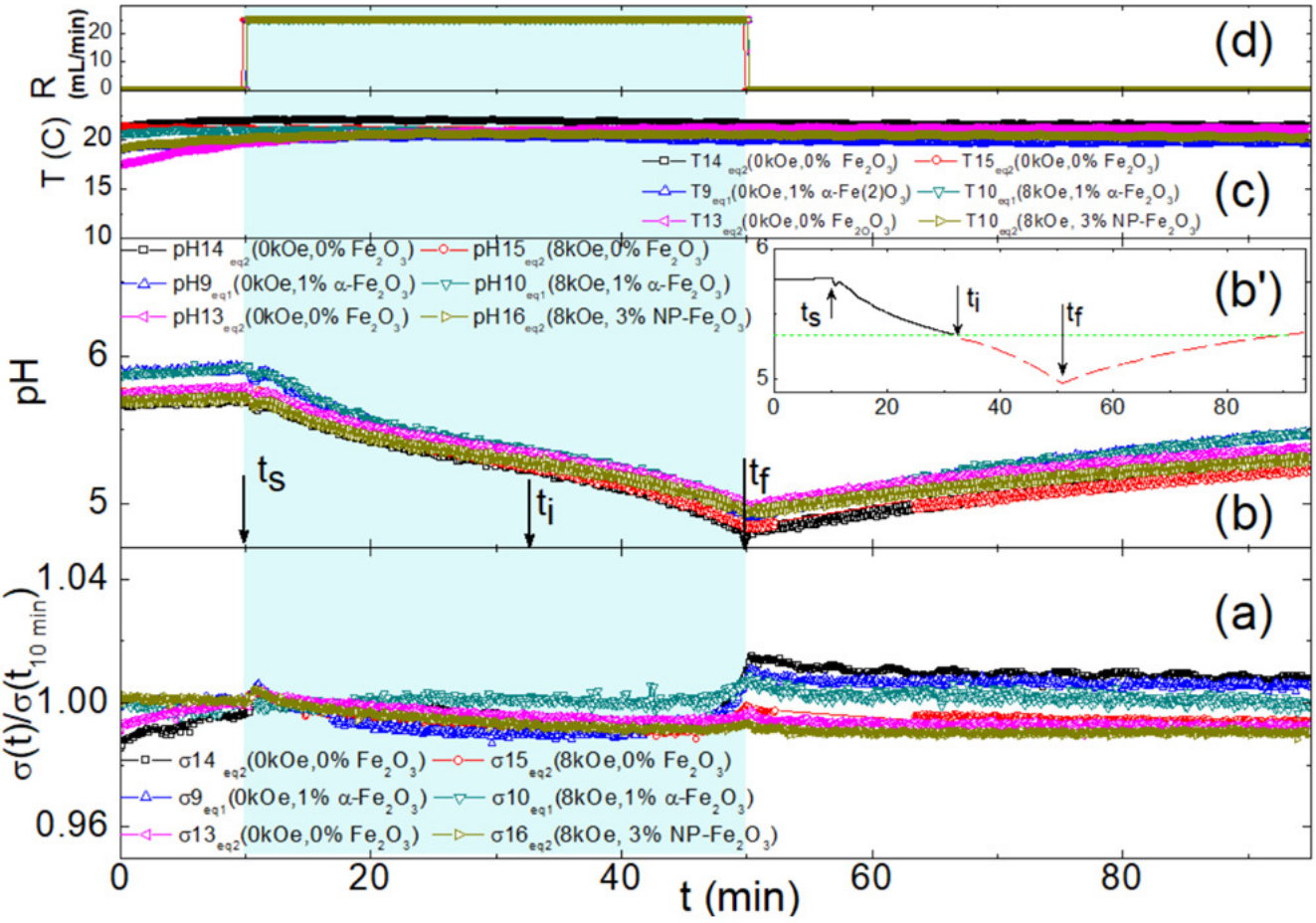

FIG. SM3. Representative conductivities and pH, all monitored *in situ* for the specified experimental conditions. **(a)** Normalized conductivity $\left(\frac{\sigma(t)}{\sigma(t_{10\,\mathrm{min}})}\right) i_{\mathrm{eq}}(\mathrm{H}, \mathrm{x\%Fe})$ for $i = 9, 10, 13-16$; eq = Eq1, Eq2; H = 0, 8.0 kOe; and x%Fe=Fe_2O_3(0, 1%), Fe_2O_3 NP(5.5%); each mixed jointly with the Ba^{2+}-based solution in the feed tank. **(b)** $\mathrm{pH}i_{\mathrm{eq}}(\mathrm{H}, \mathrm{x\%Fe})$ for the same conditions as in (a). **(c)** Average temperature from sensors shown in Fig.SM2(a). **(d)** Dosing-rate profile; the onset and duration of dosing are indicated by light-blue shading.

B. industrial-scale setup

Figure SM2(b) depicts an open-loop production line with a magnetic device at the 0 m reference position generating a strong gradient; scale powders were sampled at −1.5 m, +1.0 m, and +5331 m. Unlike the laboratory-produced scales discussed in the main text, these industrial scales contain relatively elevated Fe-bearing contaminants, enabling Fe-sensitive spectroscopies without isotopic enrichment. Accordingly, in addition to structural and magnetic measurements (see experimental setups in §II), we employed Mössbauer spectroscopy (MES) and electron spin resonance (ESR) (both *ex situ*). Room-temperature transmission Mössbauer spectra were acquired on a standard ^{57}Co/Rh Mössbauer spectrometer, while complementary room-temperature ESR spectra were recorded on a standard Bruker spectrometer. The combined datasets (XRD phase analysis, magnetometry, MES, and ESR) were used to assess the barite matrix, quantify contaminating phases, and identify the speciation and magnetic state (paramagnetic or magnetically ordered) of Fe-bearing contaminants (such a state would be of relevance to the analysis of field-gradient–mediated heterogeneous nucleation and growth).

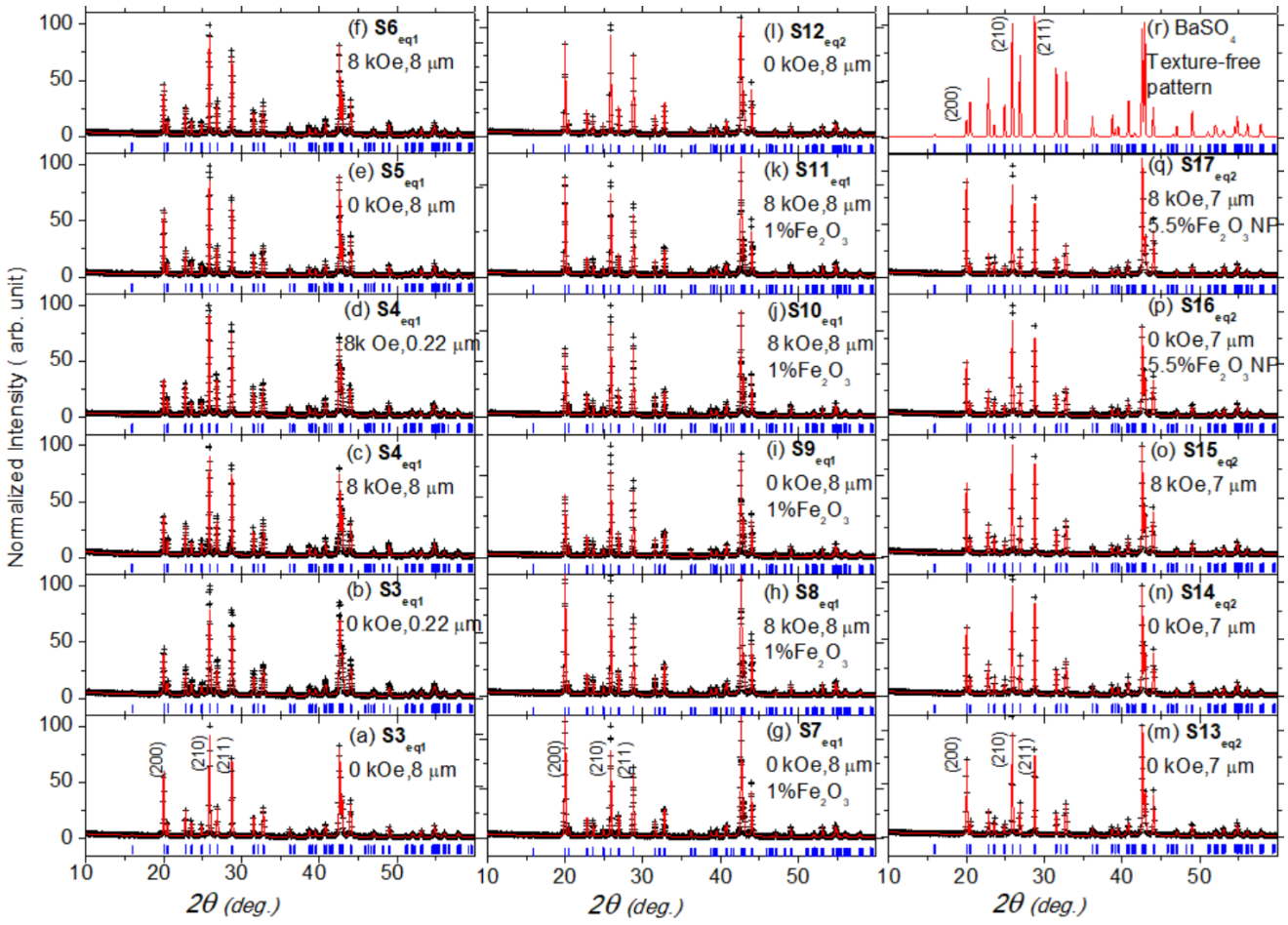

FIG. SM4. **(a-q)** X-ray diffractograms of representative residues Si_{eq}(H, x%Fe) (i=3–17). Fitted parameters are summarized in Fig.3; selected cell parameters are listed in Table SM1. **(r)** Calculated texture-free $BaSO_4$ diffractogram.[35] All intensities are normalized to the maximum of the barite (210) reflection. *Symbols*: measured intensities. *Solid lines*: Rietveld fits. *Short vertical ticks*: Bragg positions.

SM4. Complementary figures to the main text: conductivity, pH, XRD diffractograms, magnetization, susceptibility, and SEM micrographs

Below are additional conductivity/pH (Fig.SM3), XRD diffractograms (Figs.SM4-SM5), magnetization/susceptibility (Fig.SM6), and SEM micrographs (Fig.SM7) that complement the results shown and analyzed in the main text. These are mainly from the earlier runs that did not contain turbidity sensors.

SM5. Magnetic-field effects on scale formation in a production line conveying process fluid containing produced water

A. Introduction

We performed *ex situ* structural, magnetic, and microscopic analyses to assess the influence of a magnetic field on $BaSO_4$ scaling in an operational petrochemical line transporting process fluids mixed with produced water. The production-water chemistry involves downhole mixing of incompatible waters after secondary injection, promoting $BaSO_4$ formation. The ∼6 km segment of the line, Fig.SM2(b), is a scaled-up, open-loop analogue of the laboratory setup in Fig.SM2(a): in both, a supersaturated $BaSO_4$ solution flows across an applied magnetic field. Unlike the laboratory system, the industrial line includes a magnetic device, at 0 m position, that imposes a strong spatial-gradient component, $\mathbf{H}_r$, and the fluid carries a higher concentration of ferromagnetic particulates. As detailed in

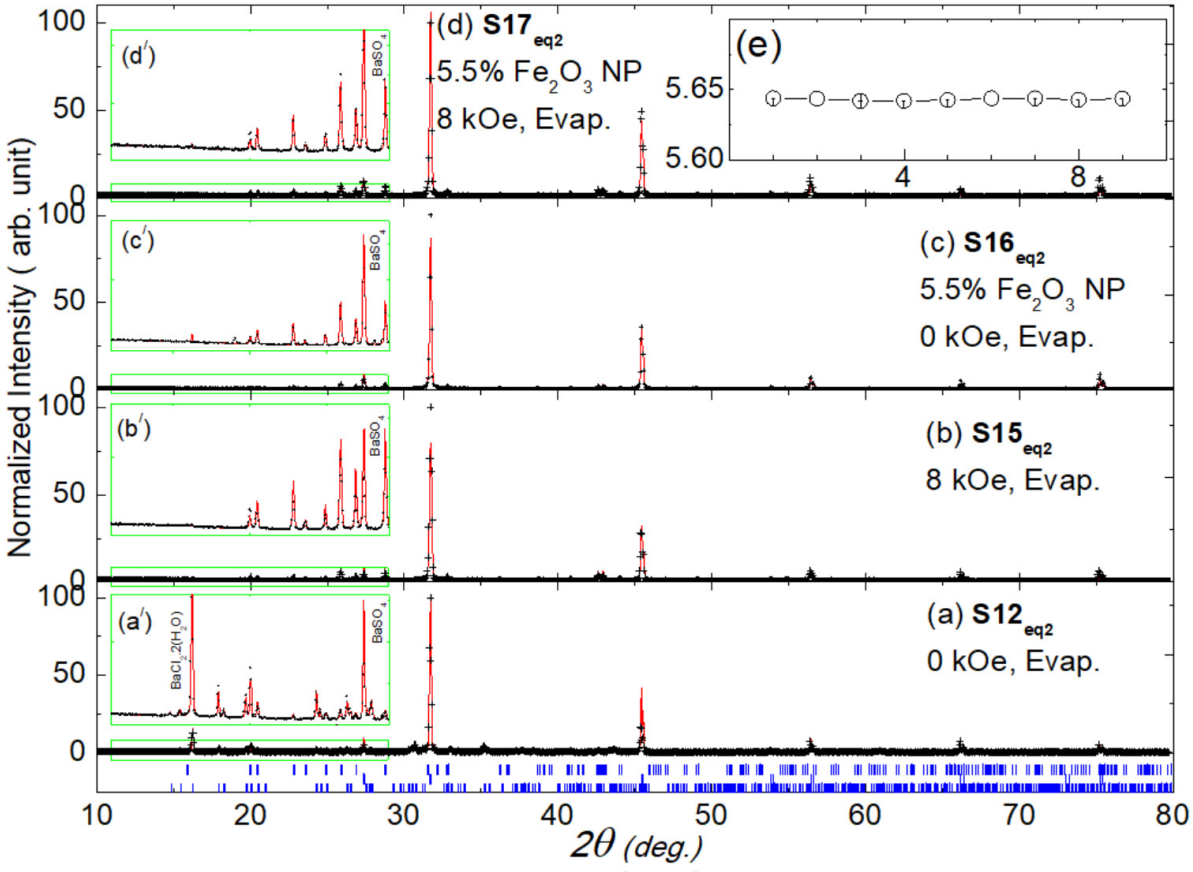

FIG. SM5. **(a-d)** X-ray diffractograms of representative evaporation residues $S_i^{eq}(H, x\%\,Fe, Evap)$ ($i = 12, 15-17$). Insets (a′-d′) highlight minor phases coexisting with the major NaCl phase: (a′) 90% NaCl, 1% $BaSO_4$, 9% $BaCl_2 \cdot 2H_2O$; (b′) 91% NaCl, 9% $BaSO_4$; (c′) 95% NaCl, 5% $BaSO_4$; and (d′) 95% NaCl, 5% $BaSO_4$. **(e)** Evolution of the NaCl lattice parameter across representative samples, confirming that its structure is scarcely affected by variations in experimental conditions. *Symbols*: measured intensities. *Solid lines*: Rietveld fits. *Short vertical ticks*: Bragg positions.

§SM1, these conditions are expected to enhance ASMT efficacy relative to laboratory experiments. To test this, we analyzed three batches—loose scale powders (with residual crude oil) collected (i) upstream (-1.5 m), (ii) near-field downstream (+1.0 m), and (iii) far downstream (+5331 m)— using XRD (§SM5 B), magnetometry (§SM5 C), and Fe-focused probes (MES and ESR; §SM5 D). A comparative discussion with the main-text results appears in §SM5 E.

B. Structural analysis

Figure SM9 compares diffractograms from the three batches; the dominant phase is $BaSO_4$ (barite).[35] A detailed structural refinement confirms that barite is the sole phase in the sample collected 1.5 m upstream of the reference location, Fig.SM9(c). In contrast, at 1.0 m downstream the barite fraction decreases to about two-thirds of its upstream value: Fig.SM9(b) yields $61 \pm 8\%$ barite, the remainder being halite. Further downstream, at 5331 m, Fig.SM9(a), the scale is composed of barite ($81 \pm 5\%$), halite ($16 \pm 4\%$), and a weak additional phase ($3 \pm 1\%$) assigned to a green-rust–type compound, $\left[Fe^{2+}_{1-x}\,Fe^{3+}_{x}\,Mg^{2+}_{y}\,(OH)_{2+2y}\right]\left[xA^-,\,mH_2O\right]^{-x}$, with $m \leq 1 - x + y$ and $A^- \in \{OH^-, Cl^-, \frac{1}{2}SO_4^{2-}, \frac{1}{2}CO_3^{2-}, HCO_3^-\}$.[37–39] Since ESR and MES measurements (see below) detect no Fe^{2+}, we restrict x to 1. This assignment is consistent with the observed color change to ochre upon prolonged air exposure (months).

Composition varied among replicate samples collected at the same location, accounting for the large standard deviations reported above; this heterogeneity—linked to turbulent flow and spatiotemporal variations in physicochemical conditions along the production line, from downhole to surface—was observed across all scale specimens.

As noted, the barite fraction decreases from 100% upstream to 61% at +1.0 m and then partially recovers to 81%

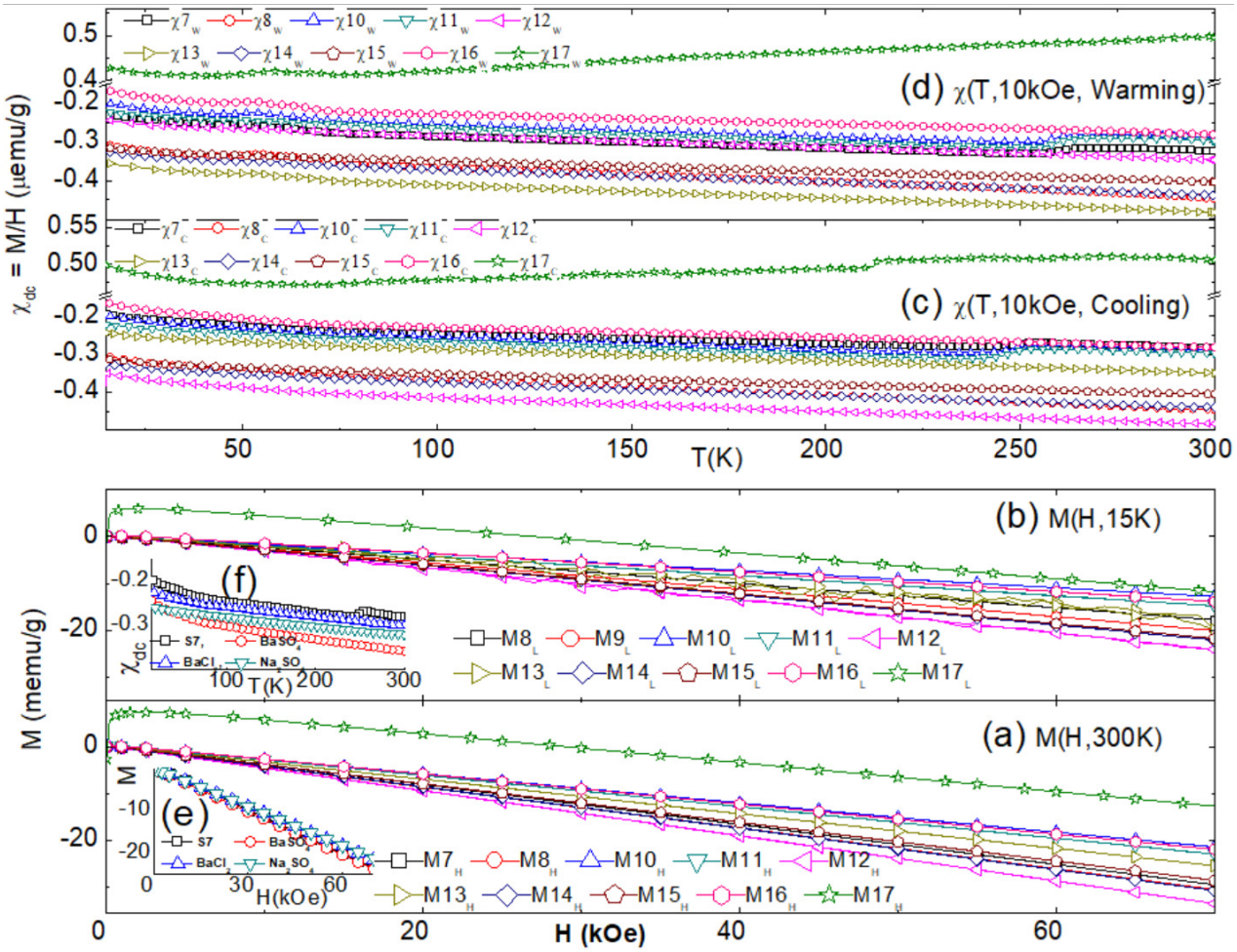

FIG. SM6. Representative magnetization isotherms $\mathrm{M}\big(\mathrm{H},\ \mathrm{T}=15,300\,\mathrm{K},\ \mathrm{S}i_{\mathrm{eq}}(\mathrm{H},\mathrm{x\%Fe},\mathrm{Filt})\big) \equiv \mathrm{M}i_{\mathrm{H/L}}$ and *dc* susceptibilities, $\chi\big(10\,\mathrm{kOe},\ \mathrm{cool/warm},\ \mathrm{S}i_{\mathrm{eq}}(\mathrm{H},\mathrm{x\%Fe},\mathrm{Filt})\big) \equiv \chi\mathrm{i}_{\mathrm{C/W}}$ when varying H, temperature, reaction route, filter pore, or type and percentage of additives (see Table SM1): **(a)** $\mathrm{M}i_{\mathrm{H}} \equiv \mathrm{M}\big(\mathrm{H},\ \mathrm{T}=300\,\mathrm{K},\ \mathrm{S}i_{\mathrm{eq}}(\mathrm{H},\mathrm{x\%Fe},\mathrm{Filt})\big)$ (i=7-8,10-17). **(b)** $\mathrm{M}i_{\mathrm{L}} \equiv \mathrm{M}\big(\mathrm{H},\ \mathrm{T}=15\,\mathrm{K},\ \mathrm{S}i_{\mathrm{eq}}(\mathrm{H},\mathrm{x\%Fe},\mathrm{Filt})\big)$ (i=7-8,10-17). **(c)** $\chi i_{\mathrm{C}} \equiv \chi\big(10\,\mathrm{kOe},\ \mathrm{cool},\ \mathrm{S}i_{\mathrm{eq}}(\mathrm{H},\mathrm{x\%Fe},\mathrm{Filt})\big)$ (i=7-8,10-17). **(d)** $\chi i_{\mathrm{W}} \equiv \chi\big(10\,\mathrm{kOe},\ \mathrm{warm},\ \mathrm{S}i_{\mathrm{eq}}(\mathrm{H},\mathrm{x\%Fe},\mathrm{Filt})\big)$ (i=7-8,10-17). **(e)** Room-temperature magnetization isotherms and **(f)** isofield susceptibility of four samples: $\mathrm{S7}_{\mathrm{eq1}}$ (squares); pure reagents $BaSO_4$ (circle), $BaCl_2$ (up triangles), and Na_2SO_4 (down triangles)

at +5331 m. We attribute these longitudinal changes to evolving physicochemical conditions along the line—most notably (i) corrosion of tubing and inserted devices (e.g., valves) and (ii) faradaic reactions[7] between the fluid and exposed internal surfaces at the site of the magnetic device—that collectively enrich Fe-bearing species and promote their downstream precipitation.

Halite appears only after passage through the strong gradient region, indicating that magnetophoretic action on suspended ferromagnetic particulates enhances heterogeneous nucleation and growth in the supersaturated halide solution. In line with the consideration of Figs.SM1(b,c), we propose core–shell entities: agglomerated ferromagnetic cores enveloped by a diamagnetic halide shell—analogous to the barite-scaling case. We assume that all barite-scale deposits were heterogeneously nucleated on dispersed contaminants. The convergence of scale compositions far downstream to barite-dominated mixtures suggests that, upon leaving the high gradient region and progressing downstream, these core–shell entities undergo partial dissolution of the halide envelope, thereby almost restoring pre-field conditions.

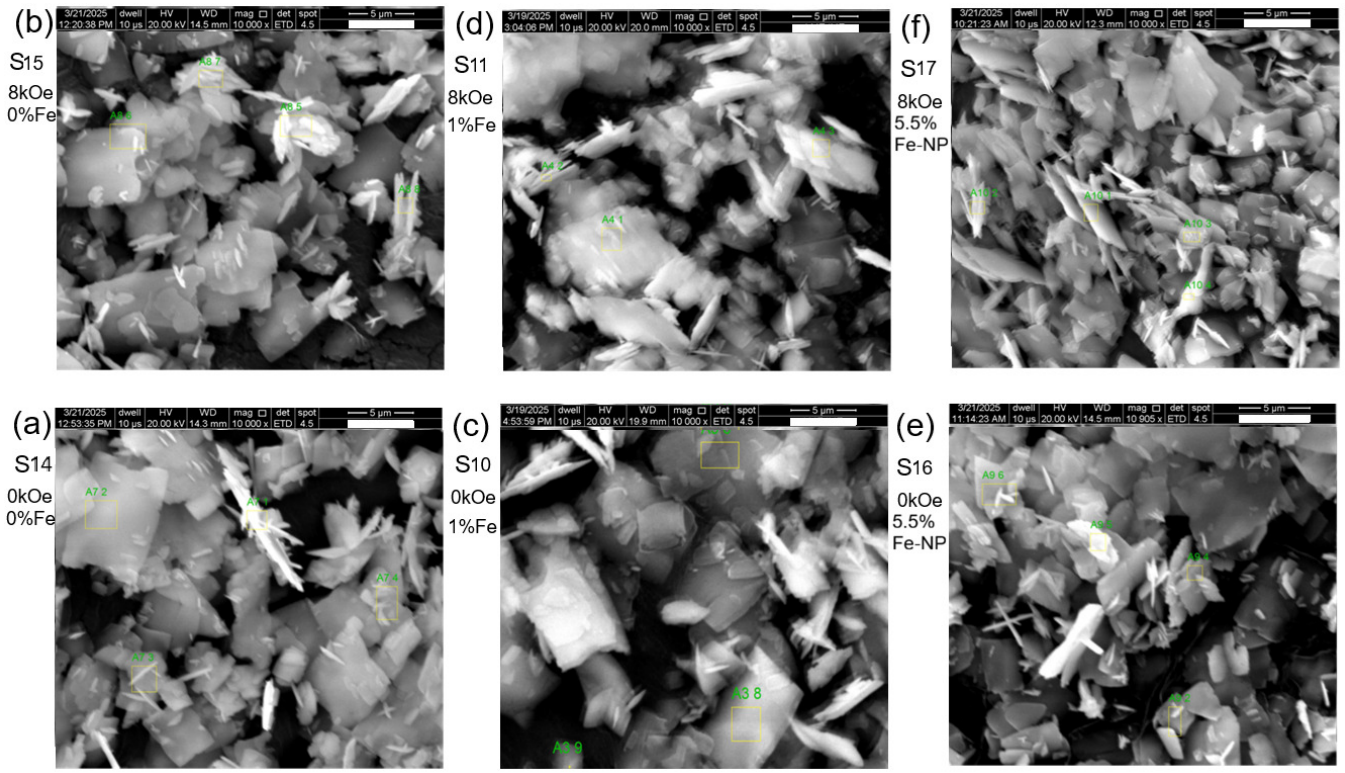

FIG. SM7. Morphologies of representative $BaSO_4$ residues (Si_{eq}(H, x%Fe, Filt) when varying H or additives. SEM micrographs of **(a)** $S14_{eq2}$(0kOe, 0%Fe, 7 μm); **(b)** $S15_{eq2}$(8kOe, 0%Fe, 7 μm); **(c)** $S10_{eq1}$(0kOe, 1%Fe_2O_3, 8 μm); **(d)** $S11_{eq1}$(8kOe, 1%Fe_2O_3, 8 μm); **(e)** $S16_{eq2}$(0kOe, 5.5%Fe_2O_3 NP, 7 μm); and **(f)** $S17_{eq2}$(8kOe, 5.5%Fe_2O_3 NP, 7 μm). The latter shows, on average, relatively dense and enhanced-size of the platelet-like forms and a diminishing concentration of of the needle-like forms. The horizontal white scale bar at the top right corresponds to 5 μm. The green alphanumeric labels mark the locations where EDS analyses were acquired. The calculated stoichiometries (normalized to Ba ion) are shown in Table SM1.

C. Magnetization analysis

Room-temperature magnetization isotherms for the three batches (Fig.SM10) show: (i) comparable coercive fields (H_c) across all samples; and (ii) remanent (M_r) and saturation (M_s) magnetizations that are comparable at –1.5 m and +5331 m, but distinctly lower at +1.0 m due to $\sim$ 40% halite dilution of the magnetically active fraction. The related M(H) curves become mutually consistent when accounting and correcting for the barite mass fraction. The similarity between the –1.5 m and +5331 m end members corroborates the XRD result that their phase assemblages are approximately alike.

As noted above, the pronounced change in phase concentration near the magnetic device is attributed to the strong gradient, ∇H, which agglomerates magnetizable particulates and creates heterogeneous nucleation sites. The accompanying rise in halite indicates that the produced water was highly saturated in NaCl and that gradient-induced agglomerates serve as templates for halide nucleation and growth.

D. Mössbauer spectroscopy and electron spin resonance analysis

The structural results in Fig.SM9—especially the phase fractions in Figs.SM9(d–e)—indicate a significant contaminating Fe-bearing component in the +5331 m samples. This motivated Fe-focused spectroscopic probes to clarify the roles of Fe-based corrosion and Fe-based magnetism in the scaling process.

Room-temperature, zero-field Mössbauer spectra for the –1.5 m, +1.0 m, and +5331 m samples (Fig.SM11) are each well described by a broadened doublet with parameters characteristic of paramagnetic Fe^{3+}.[40,41] The Fe^{3+} spectral fraction increases downstream and is largest (almost doubled) at +5331 m, consistent with progressive enrichment of Fe^{3+} along the line. The dominance of Fe^{3+} and the absence of any resolvable Fe^{2+} component point to a

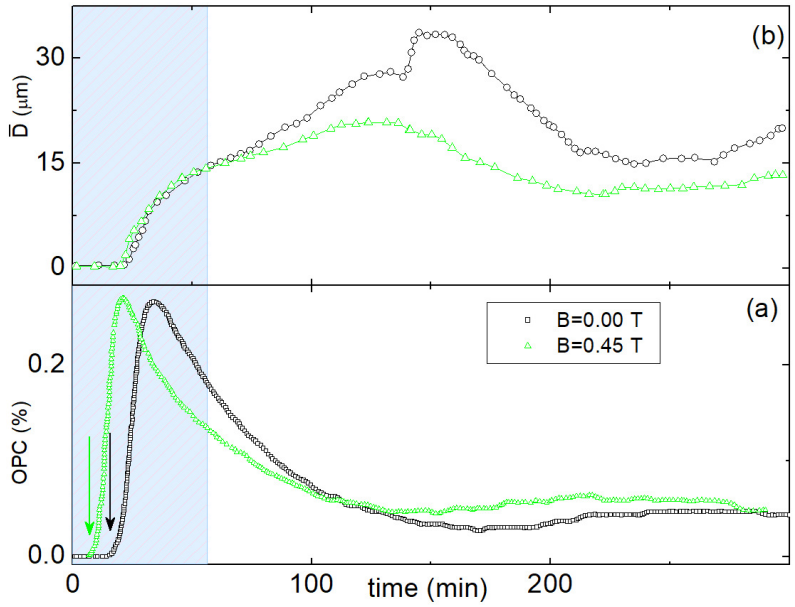

FIG. SM8. Evolution of the concentration and average diameter of precipitated $CaCO_3$ particles, as reported by Torraca[36]. The measurements were performed using an experimental setup similar, in principle, to that shown in Fig.SM2, but with the additional capability of a particle-size distribution analyzer, Sympatec™ QICPIC/LIXELL. This system allowed real-time monitoring, with and without an applied magnetic field, of (a) the concentration of precipitated $CaCO_3$ particles, expressed through the optical concentration percentage, OPC (%), and (b) their size evolution, represented by the average diameter, $\bar{D}$ (μm).

corrosive/oxidizing environment.[41]

Complementary ESR measurements, Figs.SM12(a–c), corroborate the presence of Fe^{3+} centers, exhibiting a dominant resonance with substantial linewidth, most probably due to spin–spin interactions. Notably, both ESR and MES—performed on the same powdered scale specimens used for magnetization—do not show discrete ferromagnetic signatures, such as a sharp ferromagnetic resonance in ESR or a magnetic sextet in MES. Instead, they exhibit predominantly broadened responses. This apparent disparity with the relatively strong ferromagnetic contribution inferred from the M(H) curves can be reconciled as follows:

1. *Non-Fe ferromagnetic particulates:* The FM signal in M(H) is assigned mainly to magnetic particulates whose magnetic moments are not carried by Fe. These components would therefore be absent from ^{57}Fe MES and may remain unresolved or featureless in ESR. The nearly identical saturation magnetizations, M_s, of the −1.5 m and +5331 m batches, together with the invariance of M_s despite the downstream enrichment of Fe-bearing species, support this non-Fe assignment of the ferromagnetic component. This interpretation is also consistent with the minor Fe-bearing green-rust-type phase being paramagnetic at room temperature.

2. *Sub-detection fractions of Fe-based ferromagnetic phases:* although the M(H) curves resemble those reported for iron oxides, such as hematite and magnetite, in Ref. 42, which are often associated with downhole water chemistry, the absence of corresponding hyperfine features in the MES spectra [Fig.SM11] argues against a dominant Fe-oxide origin. Rather, it suggests that any Fe-based ferromagnetic or ferrimagnetic oxide fraction is either below the ^{57}Fe hyperfine detection limit or contributes too little spectral weight to be resolved in the difference spectra.

3. *Dynamic relaxation or superparamagnetism:* an alternative possibility is that the Fe-based ferromagnetic or ferrimagnetic particulates are in a fast-relaxation, superparamagnetic regime at room temperature, so that a magnetically split MES sextet collapses into a broadened doublet. Although the observed FWHM is about twice the natural ^{57}Fe linewidth and the MES doublet parameters are compatible with rapidly relaxing Fe^{3+} environments, the broadening is more likely associated with non-ferromagnetic effects, such as site disorder or distributions of quadrupole splittings. A similar argument indicates that the ESR broadening cannot be uniquely assigned to fast superparamagnetic relaxation.

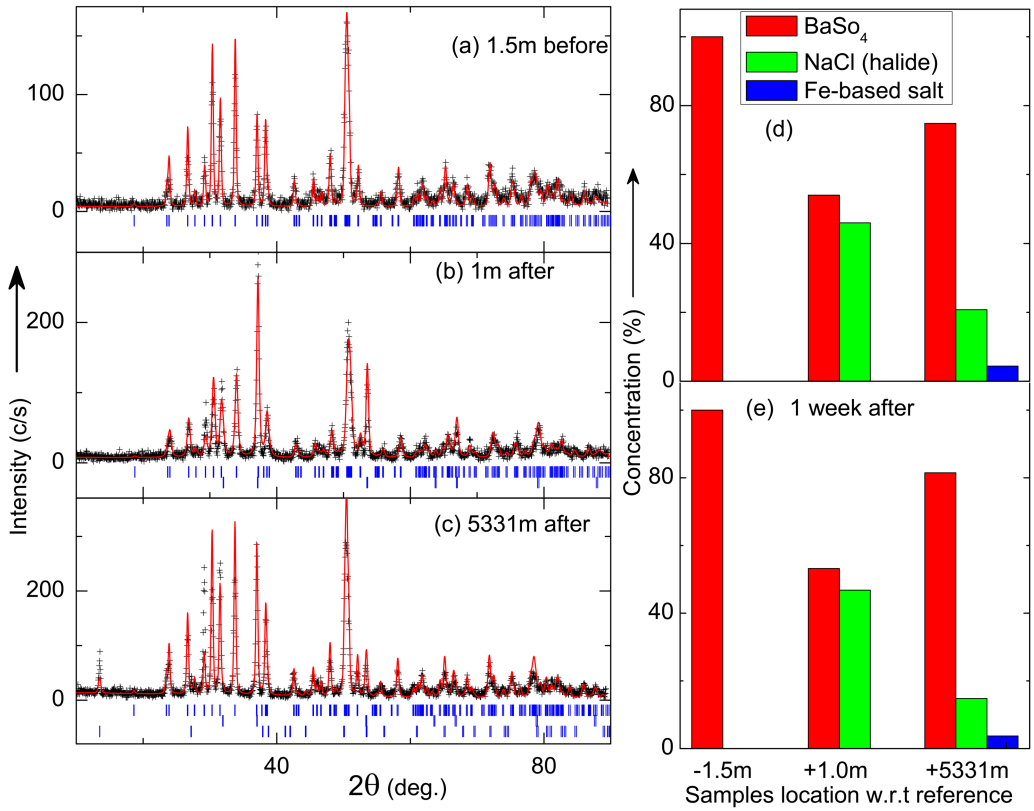

FIG. SM9. Room-temperature Co–K_α X-ray diffractograms of scales deposited at **(a)** −1.5 m, **(b)** +1.0 m, and **(c)** +5331 m relative to the reference magnetic device (located at 0 m). *Symbols* denote measured intensities; *solid lines* are Rietveld fits. *Short vertical ticks* Bragg positions (top to bottom: barite, halite, and green-rust–type). **(d)** Bar chart of the relative phase concentrations. **(e)** Bar chart showing that phase fractions remain stable after the same samples were left exposed to ambient conditions for several weeks.

Taken together, these arguments indicate that the FM signal manifested in the M(H) curves arises mainly from non-Fe particulates, which are likely coupled to the gradient-active species driving the proposed mechanism. In contrast, the Fe-specific spectroscopies mainly reveal broadened paramagnetic-like responses associated with paramagnetic Fe-based components.

It is also important to emphasize that this dichotomy applies only to the industrial case addressed here and should not be confused with the analysis of Fe-oxide contaminants discussed in the main text. In the former case, the magnetically active, non-Fe-based agglomerate templates are associated with halite scaling, whereas the main-text case concerns barite scaling assisted by Fe-oxide contaminants. Thus, both cases involve magnetophoretic modulation of scaling, but with magnetically active species of different chemical origin.

E. Discussion and conclusions

The *ex situ* analyses of the industrial scale deposits show that barite is the major phase, accompanied by contaminant phases that contribute both ferromagnetic and paramagnetic signals. The Fe-specific spectroscopies indicate that Fe occurs predominantly as Fe^{3+} and remains paramagnetic at room temperature. This response is most likely dominated by a minor Fe-bearing green-rust–type phase. Accordingly, the room-temperature ferromagnetic response observed in the magnetization curves is attributed primarily to non-Fe-based magnetic particulates.

Although a minor fraction of Fe may substitute into halite, for example on Na^+ sites with charge compensation, substitution into the Ba^{2+} sublattice of barite is disfavored by the larger ionic radius and higher coordination of Ba^{2+}. When present, Fe^{3+} is more likely to adsorb on barite crystallite surfaces; as reported for Fe^{2+}, such trace adsorbates can influence barite growth and inhibitor performance.[29–33] Taken together, the Fe signal is most consistently assigned to contaminant phases, prominently including green-rust–type compounds with x = 1.[37–39]

Pure barite is diamagnetic, but naturally occurring barite, such as that found in oil-field deposits, may contain

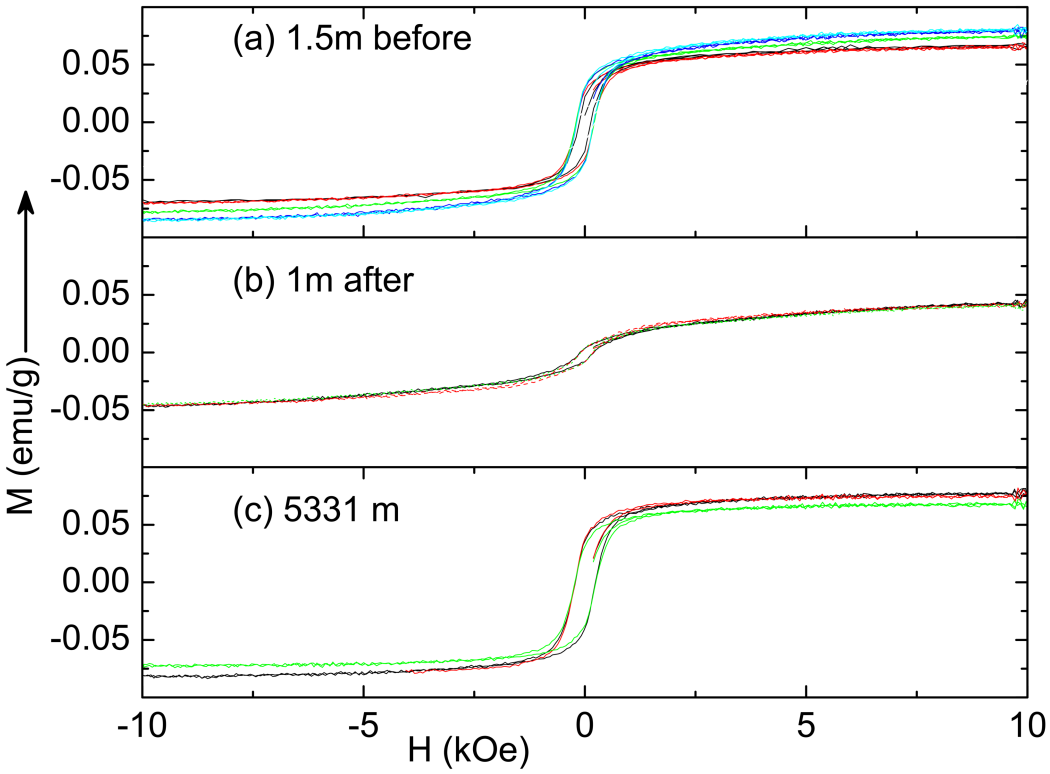

FIG. SM10. Room-temperature magnetization isotherms of different powdered scales deposited at **(a)** 1.5m before, **(b)** 1.0 m after, and **(c)** 5331 m relative to the reference magnetic device. Different colors denote magnetization of different samples that are taken from the same batch (same location); this indicates a weak inhomogeneity across the same batch.

trace magnetic ions that generate weak paramagnetic contributions. These intrinsic signals are, however, much smaller than those arising from contaminant magnetic phases, which produce the strong net response shown in Fig. SM10. This pronounced magnetic response, in contrast to the predominantly diamagnetic behavior observed in Figs. 4 and SM6, highlights the enhanced role of the magnetic-gradient force in the industrial case. In particular, the presence of ferromagnetic particulates in the produced water provides a natural basis for the strong influence of ∇H on the supersaturated NaCl scaling. It is also plausible, based on the combined XRD, MES, and ESR analyses discussed in § SM5 D, that such magnetically active particulates acted as heterogeneous nucleation templates even before exposure to the field-gradient device, possibly already in the downhole environment.

The apparent disparity between the magnetization and Fe-specific spectroscopic results is therefore reconciled as follows. The ferromagnetic signal in M(H) is assigned mainly to non-Fe-based particulates, whereas the broadened Mössbauer and ESR responses are attributed to paramagnetic Fe-bearing phases. Any Fe-based ferromagnetic contribution, if present, must either remain below the detection limit of the Fe-sensitive probes or be unresolved because of dynamic relaxation or superparamagnetic behavior. In this sense, the Fe-specific spectroscopic response is largely decoupled from the gradient-active ferromagnetic species that drive the proposed mechanism, most likely because the Fe-bearing component has a comparatively weak magnetic susceptibility.

This interpretation applies specifically to the industrial case discussed here and should not be confused with the Fe-oxide-contaminant analysis presented in the main text. In the industrial line, the magnetically active agglomerate templates are associated primarily with non-Fe-based particulates and with the modulation of halite scaling. By contrast, the main-text laboratory case concerns barite scaling assisted by Fe-oxide contaminants. Thus, both cases involve magnetophoretic modulation of scaling, but with magnetically active species of different chemical origin.

In summary, the structural, magnetic, and microscopic characterization of scale samples collected at −1.5 m, +1.0 m, and +5331 m relative to the field-gradient device shows that $BaSO_4$ remains the dominant phase, while halite increases locally near +1.0 m and barite partially recovers downstream. A minor Fe-bearing green-rust–type phase appears at +5331 m. Mössbauer and ESR measurements indicate predominantly paramagnetic Fe^{3+}, whereas the strong room-temperature ferromagnetic response is best attributed to non-Fe-based magnetic particulates. Collectively, these results support a contaminant-mediated mechanism in which the magnetic-field gradient agglomerates magnetizable

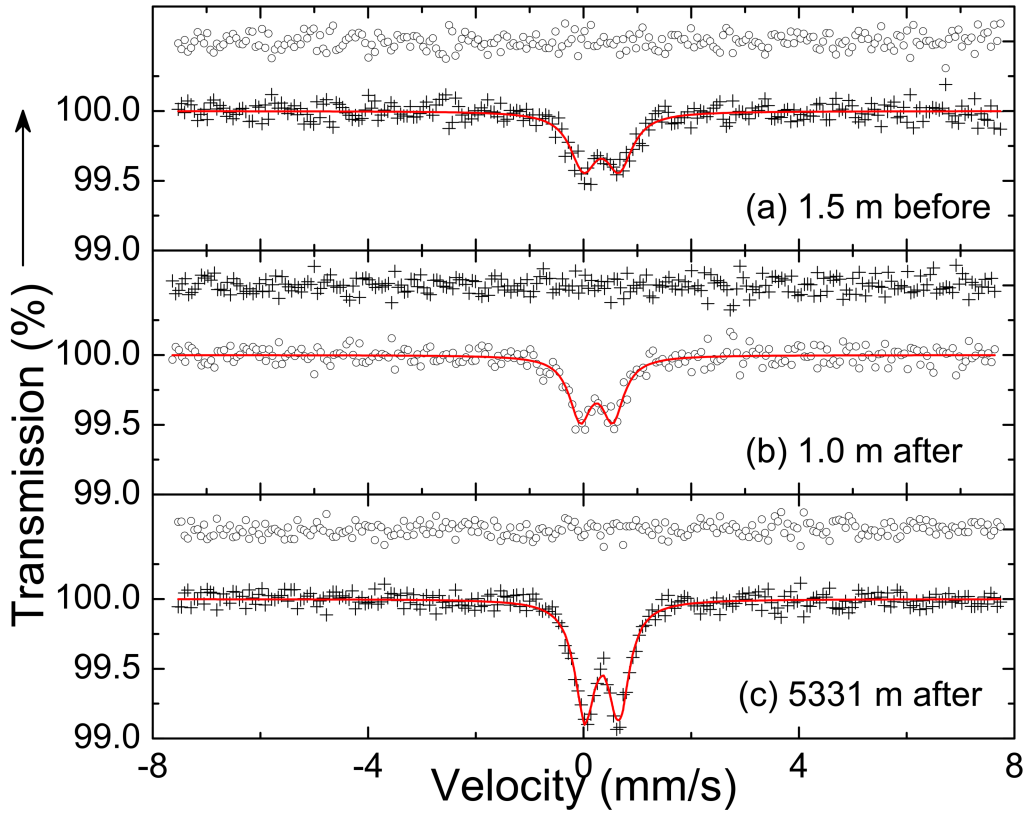

FIG. SM11. Mössbauer spectra of scale samples: **(a)** −1.5 m before (upstream), **(b)** +1.0 m after, and **(c)** +5331 m after (downstream) relative to the reference device. All room-temperature spectra are well described by a single broadened doublet with FWHM = 0.50(6) mm s^{-1}, isomer shift (IS) = 0.35(2) mm s^{-1}, and quadrupole splitting (QS) = 0.63(3) mm s^{-1}, consistent with high-spin Fe^{3+} in a paramagnetic environment.[40,41] The difference plots (circles, top of each panel) show no resolvable sextet, indicating that any ferromagnetic component lies below the MES detection limit or is dynamically relaxed at 300 K such that the sextet collapses into a broadened doublet.

particulates, creating heterogeneous nucleation sites that modulate NaCl scaling. This effect is amplified in the industrial line by the higher concentration of ferromagnetic particulates and the stronger ∇H relative to laboratory conditions.

[1] M. ElMassalami, M. Teixeira, and A. Elzubair, Investigating the antiscale magnetic treatment controversy: Insights from the model calcium carbonate scalant, Sc. Rep. **15**, 3441 (2025).
[2] (), For a weakly diamagnetic fluid with negligible bulk magnetization, $\mathbf{B} = \mathbf{H} + 4\pi\mathbf{M} \simeq \mathbf{H}$.
[3] E. J. Williams, The induction of electromotive forces in a moving liquid by a magnetic field, and its application to an investigation of the flow of liquids, Proc. Phys. Soc. **42**, 466 (1930).
[4] R. De Luca, Lorentz force on sodium and chlorine ions in a salt water solution flow under a transverse magnetic field, Eur. J. Phys. **30**, 459 (2009).
[5] T. A. Butcher and J. Coey, Magnetic forces in paramagnetic fluids, Journal of Physics: Condensed Matter **35**, 053002 (2022).
[6] L. M. Monzon and J. Coey, Magnetic fields in electrochemistry: The kelvin force. a mini-review, Electrochemistry Communications **42**, 42 (2014).
[7] M. ElMassalami, M. Teixeira, H. Schluter, and A. Martins, Magneto-electric induction in a magnetically-uncontaminated supersaturated aqueous solution flowing through an open-circuit faraday-type electrolytic cell, Int. J. Electrochem. Sci. **21**, 101434 (2026).
[8] J. A. Fleming, On magneto-electric induction in liquids and gases.—Part I. production of induced currents in electrolytes, Proc. R. Soc. Lond. **26**, 40 (1878).
[9] A. Kolin, An alternating field induction flow meter of high sensitivity, Rev. Sci. Instrum. **16**, 109 (1945).

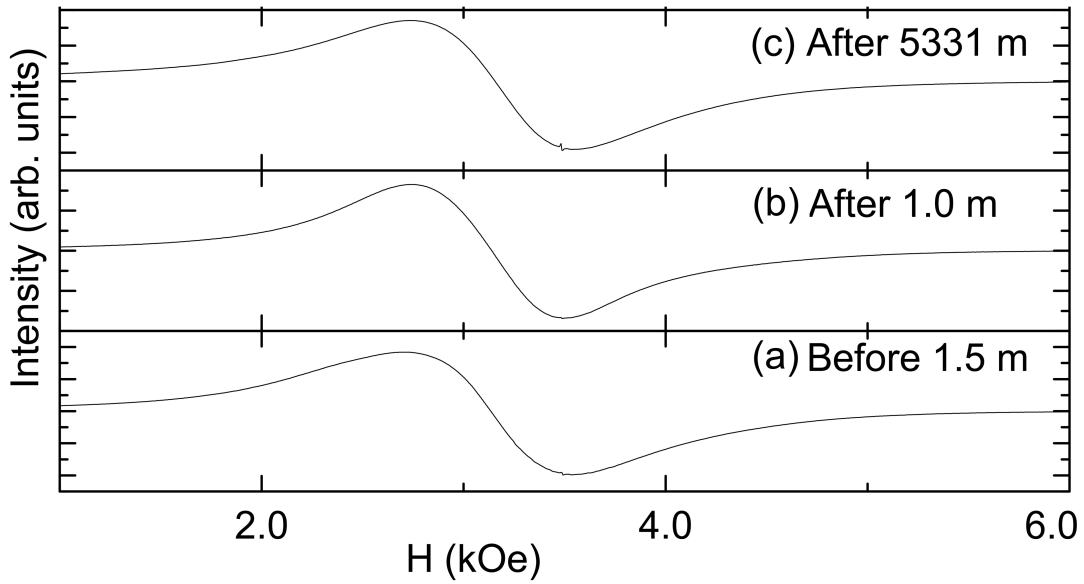

FIG. SM12. Room-temperature ESR spectra of scale samples: **(a)** −1.5 m (upstream), **(b)** +1.0 m, and **(c)** +5331 m (downstream) relative to the reference device. In all cases, the dominant resonance arises from Fe^{3+} centers; the broad linewidth is consistent with significant spin–spin interactions, indicating that the Fe^{3+} ions are not widely separated on the ESR characteristic scale.

[10] D. B. Geselowitz, Comment on the Hall effect in a flowing electrolyte, Proc. Phys. Soc. **40**, 1183 (1972).
[11] J. J. Wright and S. Van Der Beken, The Hall Effect in a Flowing Electrolyte, Am. J. Phys. **40**, 245 (1972).
[12] K. W. Busch, M. A. Busch, D. H. Parker, R. E. Darling, and J. L. McAtee, Jr., Studies of a water treatment device that uses magnetic fields, Corrosion **42**, 211 (1986).
[13] M. Szwast and W. Piatkiewicz, Hall effect in electrolyte flow measurements: introduction to blood flow measurements, Artif. Organs **36**, 551 (2012).
[14] A. Di Lieto, A. Giuliano, F. Maccarrone, and G. Paffuti, Hall effect in a moving liquid, Eur. J. Phys. **33**, 115 (2011).
[15] I. V. Markov, *Crystal growth for beginners: fundamentals of nucleation, crystal growth and epitaxy*, 3rd ed. (World scientific, 2016) ISBN: 978-9813143425.
[16] J. Kawano, N. Shimobayashi, A. Miyake, and M. Kitamura, Precipitation diagram of calcium carbonate polymorphs: its construction and significance, J. Phys.: Condens. Matter **21**, 425102 (2009).
[17] P. Dunne, L. Mazza, and J. M. D. Coey, Magnetic structuring of electrodeposits, Phys. Rev. Lett. **107**, 024501 (2011).
[18] M. Waskaas, On the origin of the magnetic concentration gradient force and its interaction mechanisms with mass transfer in paramagnetic electrolytes, Fluids **6**, 114 (2021).
[19] (), magnetophoretic agglomeration is fundamentally distinct from electrostatic flocculation. The former is a field-gradient-driven assembly of magnetizable particles arising from magnetic forces, analogous to the organization of iron filings in the vicinity of a bar magnet. It typically promotes the formation of aligned chains or columnar structures, although, for simplicity, it is represented schematically as quasi-spheroidal aggregates in Fig. SM1(b,c).
[20] P.-L. Lee, E. Huang, and S.-C. Yu, Phase diagram and equations of state of baso4, International Journal of High Pressure Research **21**, 67 (2001).
[21] P.-L. Lee, E. Huang, and S.-C. Yu, High-pressure Raman and X-ray studies of barite, $BaSO_4$, High Pressure Research **23**, 439 (2003).
[22] W. A. Crichton, M. Merlini, M. Hanfland, and H. Muller, The crystal structure of barite, $BaSO_4$, at high pressure, American Mineralogist **96**, 364 (2011).
[23] S. Mann, The chemistry of form, Angewandte Chemie International Edition **39**, 3392 (2000).
[24] S. Rajam and S. Mann, Selective stabilization of the (001) face of calcite in the presence of lithium, J. Chem. Soc., Chem. Commun. , 1789 (1990).
[25] M. Yokota, E. Oikawa, J. Yamanaka, A. Sato, and N. Kubota, Formation and structure of round-shaped crystals of barium sulfate, Chemical Engineering Science **55**, 4379 (2000).
[26] D. Kashchiev and G. Van Rosmalen, Nucleation in solutions revisited, Crystal Research and Technology: Journal of Experimental and Industrial Crystallography **38**, 555 (2003).
[27] D. Gunn and M. Murthy, Kinetics and mechanisms of precipitations, Chemical Engineering Science **27**, 1293 (1972).
[28] M. Murthy, Theory of crystal growth in phase transformations: precipitation of barium sulphate, Chemical engineering

science **49**, 2389 (1994).

[29] Z. Zhang, F. Zhang, Q. L. Wang, N. Bhandari, F. Yan, Y. Liu, Z. Dai, L. Wang, V. Bolanos, A. T. Kan, *et al.*, Ferrous iron impact on phosphonate and polymeric scale inhibitors at temperature ranging from 25 to 70°C, in *SPE International Conference on Oilfield Chemistry* (SPE, 2015) p. D011S002R008.

[30] Z. Zhang, *Impact of Fe (II) and Fe (III) on scale inhibitor: application to scale control in oil and gas systems*, Ph.D. thesis, Rice University (2017).

[31] S. Gaffney, E. Jackson, and A. Lyons, The effect of lron (ii) on the barium sulphate scale inhibition performance of diethylenetriaminepentamethylene phosphonic acid (detpma), in *Symposium on Chemicals in the Oil Industry, London, England* (1988).

[32] J. Coleman, G. Graham, S. Dyer, P. Hill, and K. Sorbie, Iron release following scale inhibitor application and mineral dissolution in a north alsakan reservoir-some field implications, in *SPE International Symposium on Formation Damage Control, Aberdeen, UK* (1999) paper # SPE-58727-MS.

[33] L. S. Stoppelenburg and M. Yuan, The performance of barium sulfate inhibitors in iron containing waters in both aerated and anaerobic systems, in *Corrosion 2000* (Association for Materials Protection and Performance, 2000) p. 1.

[34] A. Paykani and H. Mardan, Methods of controlling ferric hydroxide precipitation results from corrosion in acidizing treatments (2016).

[35] Inorganic crystal structure data base, www.fiz-karlsruhe.de/de/leistungen/kristallographie/icsd.html (2025).

[36] J. R. Torraca Neto, *Study of calcium carbonate formation under the influence of magnetic fields*, Master's thesis, Escola de Química, Universidade Federal do Rio de Janeiro (2018), in portugues.

[37] J.-M. R. Génin, R. Aissa, A. Géhin, M. Abdelmoula, O. Benali, V. Ernstsen, G. Ona-Nguema, C. Upadhyay, and C. Ruby, Fougerite and Fe^{II-III} hydroxycarbonate green rust; ordering, deprotonation and/or cation substitution; structure of hydrotalcite-like compounds and mythic ferrosic hydroxide $Fe(OH)_{(2+x)}$, Solid State Sciences **7**, 545 (2005).

[38] F. Trolard and G. Bourrié, Structure of fougerite and green rusts and a thermodynamic model for their stabilities, Journal of Geochemical Exploration **88**, 249 (2006).

[39] F. Trolard, G. Bourrié, M. Abdelmoula, P. Refait, and F. Feder, Fougerite, a new mineral of the pyroaurite-iowaite group: Description and crystal structure, Clays and Clay Minerals **55**, 323 (2007).

[40] T. C. Greenwood and N. N. Gibb, *Mossbauer Spectroscopy* (Chapman and Hall Ltd. London, 1971).

[41] D. Gallup and W. Reiff, Characterization of geothermal scale deposits by ^{57}Fe Mössbauer spectroscopy and complementary X-ray diffraction and infra-red studies, Geothermics **20**, 207 (1991).

[42] S. A. A. Imhmed, *Application of magnetic susceptibility measurements to oilfield scale management*, Ph.D. thesis, Heriot-Watt University (2012).